Songklanakarin J. Sci. Technol.
40 (6), 1456-1463, Nov. - Dec. 2018

http://www.sjst.psu.ac.th

Original Article

Combustion of microalgae *Nannochloropsis oculata* biomass: cellular macromolecular and mineralogical content changes during thermal decomposition

Sukarni Sukarni[1*], Uun Yanuhar[2], I. N. G. Wardana[3], Sudjito Sudjito[3], Nurkholis Hamidi[3], Widya Wijayanti[3], Yusuf Wibisono[4], Sumarli Sumarli[1], I. M. Nauri[1], and Heru Suryanto[1]

[1] *Center for Renewable and Sustainable Energy Engineering, Department of Mechanical Engineering, Faculty of Engineering, State University of Malang, Malang, 65145 Indonesia*

[2] *Biotechnology Laboratory, Department of Water Resources Management, Faculty of Fisheries and Marine Sciences, University of Brawijaya, Malang, 65145 Indonesia*

[3] *Department of Mechanical Engineering, Faculty of Engineering, University of Brawijaya, Malang, 65145 Indonesia*

[4] *Bioprocess Engineering, Department of Agricultural Engineering, Faculty of Agricultural Technology, University of Brawijaya, Malang, 65145 Indonesia*

Received: 5 March 2017; Revised: 5 September 2017; Accepted: 12 September 2017

Abstract

The cellular macromolecular and mineralogical content changes during the combustion of *Nannochloropsis oculata* biomass have been investigated. A Fourier transform infrared spectroscopy (FTIR) analyzer was used to investigate the cellular macromolecular content changes of biomass at every stage of decomposition during heating to 1200 ˚C. From ambient temperatures to 190 ˚C, similar spectra were obtained, indicating relatively little change in the chemical structure of the biomass material. Changes in the spectra are very noticeable from 190 to 1200 ˚C. The combustion process begins with thermal cracking of the –OH groups of silanol that escape together with moisture at temperatures up to 190 ˚C. Subsequent temperature increase decreased intensity of the spectrum, indicating thermal degradation of the organic compounds derived from lipids, proteins, and carbohydrates. These processes occur up to 800 ˚C. The X-ray diffraction (XRD) results showed that the mineral constituents of biomass degraded during the combustion process, and a portion reacted to form new compounds such as *melilite* ($Ca_6Na_2O_{15}Si_4$). The SEM images show a morphological distinction between biomass and its residue at 1200 ˚C, due to the decomposition and rearrangement of the mineral content during heating. Fragmentation of the samples also occurred during heating, characterized by more uniform residue at 1200 ˚C.

Keywords: combustion, microalgae, *Nannochloropsis oculata*, cellular macromolecular, mineralogical content

*Corresponding author
Email address: sukarni.ft@um.ac.id

1. Introduction

Renewable and clean energy has been investigated for replacing fossil fuels in the interests of sustainable energy and the global environment. Microalgae are comparable to other renewable energy sources in terms of the abundance and production rate. Per unit area, the energy produced by microalgae is 30-100 times greater than that of terrestrial crops (Demirbas, 2010). microalgae applications in energy can have a zero net CO_2 emissions because the carbon that is in the form of CO_2 is fixed via photosynthesis during the growth of microalgae. Approximately 1.83 tons of CO_2 are consumed by 1 ton of algal biomass during its cultivation (Yusuf, 2007); hence, massive production of microalgal biomass would significantly contribute to global warming mitigation, and the utilization of microalgal biomass in existing power plants is very appealing.

One of the microalgae species that has been proposed as an excellent candidate for biofuel feedstock is *Nannochloropsis oculata* (*N. oculata*) (Griffiths & Harrison, 20 09). This microalga belongs to the *Eustigmatophyceae* class, and is unicellular small green alga characterized by coccoid forms with a diameter of 2-5 μm (Hu & Gao, 2003). These species do not contain chlorophyll *b* (Hibberd, 1981) or cellular xanthophyll pigments. The cell walls are present, composed of fibrillar and amorphous components. Cellulose, a polymer of 1,4 linked β-D-glucose, is the most common fibrillar component. The fibril part is embedded in an amorphous mucilaginous material composed of polysaccharides, proteins, and lipids. Occasionally, calcium carbonate, silica, or sporopollenin, which are extraordinarily resistant materials, are also present as encrusting substances (Barsanti & Gualtieri, 2006). There is chloroplast without girdle lamella and outer chloroplast endoplasmic reticulum membrane with a direct membrane connection to the outer nuclear envelope membrane. These species are commonly cultivated in aquaculture industries to rear aquatic animals, especially live food organisms such as rotifers.

The potential of *N. oculata* as a solid fuel feedstock in terms of its abundance and physicochemical properties was demonstrated previously (Sukarni, Sudjito, Hamidi, Yanuhar, & Wardana, 2014). It is clear that with traditional natural and low-cost nutrient cultivation, the productivity of this algae is higher than that of *Dunaliella salina* (García-González, Moreno, Manzano, Florencio, & Guerrero, 2005), *Scenedesmus obliquus* (de Morais & Costa, 2007), or *Chlorella vulgaris* (Converti, Casazza, Ortiz, Perego, & Del Borghi, 2009). This strain is a viable candidate for providing a continuous supply of renewable solid fuel feedstock.

Recently, very few studies have focused on microalgal combustion. López-González, Fernandez-Lopez, Valverde, and Sanchez-Silva (2014) studied the thermal characteristics of three different microalgae species: *Nannochloropsis gaditana, Scenedesmus almeriensis* and *Chlorella vulgaris*, under oxidizing conditions using thermogravimetric analysis and differential scanning calorimetry (TGA–DSC). The results indicated that two main stages of microalgae combustion occurred during thermal degradation, i.e., devolatilization and char oxidation. Tahmasebi, Kassim, Yu, and Bhattacharya (20 13) investigated the co-combustion behavior and reaction kinetics of *Tetraselmis suecica* microalgae in a blend with Victorian brown coal, in O_2/N_2 and O_2/CO_2 atmospheres using the thermogravimetric method. During combustion of microalgae, two peaks at 265 and 485 ˚C were found, in agreement with the combustion of protein or carbohydrate with lipid, respectively. Chen, Ma, and Liu (2011) investigated the combustion characteristics of *Chlorella vulgaris* under different oxygen concentrations and found that the combustion process of this algae can be divided into three stages. Furthermore, in our previous paper (Sukarni, Sudjito, Hamidi, Yanuhar, & Wardana, 2015) we examined the combustion of *N. oculata* biomass and showed that this algae decomposed in five stages during thermal treatment from ambient temperature to 1200 ˚C. Overall, the previous research was concerned with the thermal decomposition behavior of the algal biomass, and it was determined that there are differences in the thermal decomposition stages between the various algae species, probably due to differences in their compartmental contents. However, to the best of our knowledge, the details of macromolecular and mineralogical changes due to elevated temperatures during combustion have not been investigated, and the residue morphology and chemical composition have not been studied. Hence, to facilitate the use of this biomass with appropriate combustion technology and potential applications of its unique waste ashes, further in-depth research is required.

This article presents a study of the thermal decomposition of *N. oculata* biomass in terms of macromolecular and mineralogical content changes as functions of temperature, to describe the step-by-step decomposition of biomass elements. The characteristics of biomass and its residue at 1200 ˚C were also examined as regards their morphology and composition.

2. Materials and Methods

2.1 Material and its physicochemical properties

The details of culturing, harvesting, drying and preparing microalgal biomass have been reported elsewhere (Sukarni *et al*., 2014, 2015). The original of *N. oculata* species was prepared by the Institute of Brackish Water Aquaculture (Balai Budidaya Air Payau-BBAP) Situbondo, East Java, Indonesia. An open pond filled with 8 m^3 filtered sterilized seawater with pH and salinity of 8.6 and 34 ‰, respectively, and enriched with 0.1% (v/v) Walne's fertilizer, was used for sample culturing. The fertilizer composition was KNO_3=1 kg, NaH_2PO_4=100 g, Na_2 EDTA=100 g, $FeCl_3$=13 g, dissolved in 10 liters of water. The algae were cultured for 7 days and then harvested.

Chemical flocculation was performed with caustic soda (NaOH) for microalgal biomass harvesting. The precipitation occurred overnight, and then the sample was filtered and washed with distilled water. In due course, the collected sediment was dried in an oven at 80 ˚C for 24 h, to get dry algal chunks. A fine algal powder (1.75 kg) was obtained by crushing the dried chunks using a mortar. Subsequently, this powder was stored in a vacuum desiccator to keep it dry.

Algal biomass physicochemical properties as regards chemical composition, proximate analysis results, and the heating value, are presented in Table 1. These data are quoted from Sukarni *et al*. (2014).

Table 1. Physicochemical properties of *N. oculata* biomass (quoted from Sukarni *et al*. (2014))

EDX analysis (wt%)								Proximate analysis (% by dry basis)			HHV (MJ/kg)
C	O	Na	Mg	Al	Si	Cl	Ca	Volatile matter	Fixed carbon	Ash	
28.32	43.80	2.04	13.16	0.92	1.60	1.97	8.20	67.45	8.08	24.47	16.80

2.2 Thermal analysis method and the residual characterization

Thermogravimetric (TG) and derivative thermogravimetric (DTG) analysis were conducted using STA PT1600 (Linseis STA Simultaneous Thermal Analysis, Germany). The sample with an initial weight of 20 mg was loaded into an Al_2O_3 ceramic crucible and heated at a rate of 10 ˚C/min from ambient temperature to 1200 ˚C. A constant air flow rate of 100 ml/min was passed through the sample chamber.

In the TG and DTG curves from thermogravimetric experiments, the decomposition temperature for each stage could be determined. The overall characteristic parameters determined include the approximate starting and ending points of DTG curve changes, indicating the elemental components in the samples undergoing thermal breakdown. These parameters were presented in Sukarni *et al*. (2015).

Based on the characteristic parameters, a new sample was heated in a STA Thermal Analyzer to perform each stage of decomposition in a controlled way, and then the residual material was analyzed using Fourier transform infrared spectroscopy (FTIR) and X-ray diffraction (XRD) to determine chemical macromolecular compounds and mineralogical changes, respectively. The morphological changes in biomass and residue at 1200 ˚C were studied by scanning electron microscopy (SEM), and the chemical elements were analyzed using energy-dispersive X-ray (EDX) spectrometry. The FTIR technique, as well as the EDX method, have been presented elsewhere (Sukarni *et al*., 2014).

2.3 FTIR analysis

Shimadzu FTIR spectroscopy was used to investigate the infrared spectra of dried algal biomass and its residue. Potassium bromide (KBr) powder was mixed with each sample and then pressed into tablets before measurement. Scanning of the samples was performed from 400 to 4,000 cm^{-1}.

2.4 Energy-dispersive X-ray (EDX) spectrometry

The EDX spectrometry for determining the elemental composition of algal biomass and its residue at 1200 ˚C were conducted with an FEI Inspect S50 equipped with X-ray microanalysis capabilities (AMETEK EDAX^{TSL}). Gold coating the samples was done prior to analysis to minimize image distortion by accumulation of electric charges, and the images were recorded and evaluated. For each sample, 3 points or area EDX analyses were performed, and then the results were averaged.

2.5 SEM (Scanning Electron Microscopy)

To determine the physical distinctions between biomass raw material and the residue at 1200 ˚C in terms of morphology, a scanning electron microscope (SEM) was used. An imaging SEM (Inspect-S50-type, FEI scanning electron microscope) was employed to take sample images at four magnifications: 4,000×, 5,000×, 7,000×, and 10,000×. The images of biomass and residue at 1200 ˚C, 7,000× and 10,000×, are included in this paper.

2.6 XRD analyses

XRD patterns for identifying the mineral composition of each sample were obtained using a PAN Analytical X'Pert Pro Diffractometer system with CuKα radiation (λ= 1.54 Å). Samples were scanned with a goniometer from 10° to 90° (2θ angle range) in 0.02° steps at 40 kV and 30 mA. Peak identification was done with the PANanalytical X'Pert HighScore Plus software package.

3. Results and Discussion

3.1 Cellular macromolecular content changes

The decomposition profile of a 20 mg sample is shown by the TG and DTG curves in Figure 1. The onset of initial volatilization stage was at approximately 190 ˚C and it

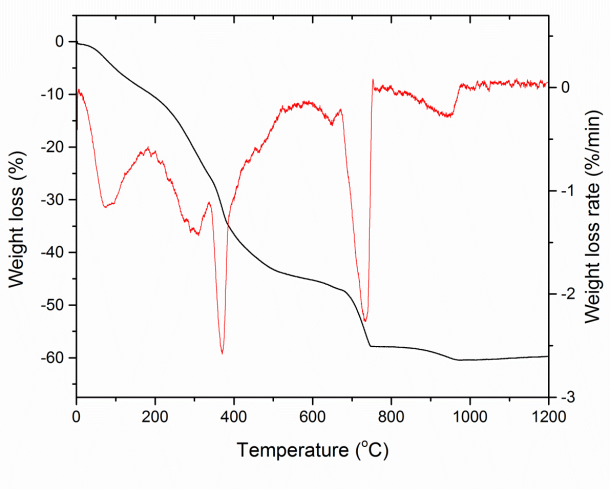

Figure 1. TG and DTG curves of *N.oculata* combustion at 10 ºC/min (adapted from Sukarni et al., (2015)).

was terminated at 461 ˚C. This was followed by a transition stage in which the remaining volatiles and char burned simultaneously, reaching completion at 673 ˚C. Subsequently, char decomposition and oxidation stage occurred, and this was completed at approximately 762 ˚C. These completion temperatures were used to study the macromolecular and mineralogical changes in the sample.

The macromolecular content change of the sample at each stage of biomass decomposition was observed from FTIR spectra, by heating the sample from ambient temperature to the end of each stage according to Figure 1. Figure 2 shows the FTIR spectra of the samples, each of which was obtained from the decomposition of 20 mg of biomass at a 10 °C/min heating rate.

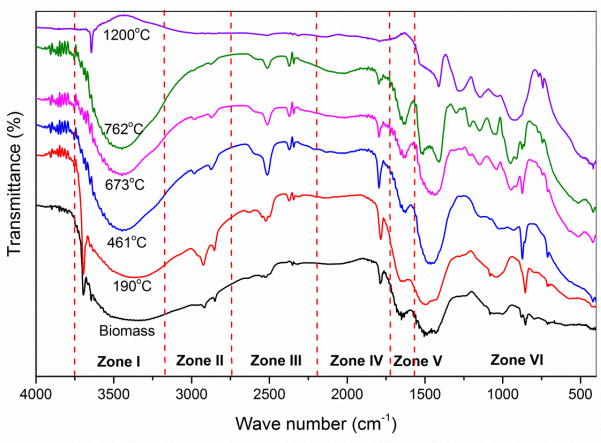

Figure 2. FTIR spectra of *N. Oculata* biomass and residue after heating to various temperatures.

As shown in Figure 2, the change of the cellular macromolecular content at each stage of decomposition was determined from bands in the range from 4000 to 400 cm^{-1}. The assignment of these bands to specified macromolecular changes was done tentatively on the basis of biochemical reference standards and published FTIR spectra as quoted in our previous work (Sukarni *et al*., 2014).

The peak at 3694 cm^{-1} resulted from the O−H stretching of silanol and adsorbed water bonded to silica in the cell wall, which was lost when heating to over 190 ˚C. This indicates that most of the H_2O and –OH groups first escape from the sample particles at a temperature above 190 ˚C, which is consistent with the results obtained for samples of rice straw (Peng *et al*., 2009) and oil shale (Chen, Han, & Jiang, 2016), which released H_2O and –OH groups at approximately 200 ˚C. However, a similar peak appeared at 1200 ˚C. This might be due to the absorption of water while ash was transferred from the combustion chamber to the desiccator, considering that silica is a hydrophilic element. The extensive IR band in Zone I remained stable up to 762 ˚C and disappeared at 1200 ˚C. This band was due to proteins, i.e., the N–H bond in the amide A group (Duygu *et al*., 2012).

The two weak peaks at 2916 and 2849 cm^{-1} (Zone II) gradually weakened with increasing temperature, and they disappeared above 673 ˚C. This revealed a methylene group in the lipid that decomposed above this temperature. The featured band at 2523 cm^{-1} (Zone III), associated with the $-NH_3^+$ group of a protein, became weaker at 762 ˚C and vanished at 1200 ˚C.

The spectral band at 1788 cm^{-1} (Zone IV) was weak at 762 ˚C and subsequently disappeared at 1200 ˚C. This was attributed to the C=O group of an ester, which is present in fatty acids or proteins. In Zone V, the pronounced band at 1651 cm^{-1} was associated with C=O stretching of amide I. It remained constant in intensity up to 673 ˚C, declined above 762 ˚C and then vanished at 1200 ˚C.

The band at 1504 cm^{-1} shifted at 762 ˚C and 1200 ˚C toward 1409 cm^{-1}. This was mainly due to C–H stretching and N–H bending modes of protein amide II. Subsequent heating caused a rearrangement of chemical bonds and formation of new compounds. The transmission band at 1409 cm^{-1} was due to calcium carbonate (Bellamy, 1975).

Many bands in Zone VI with various peaks were associated with inorganic elements, such as phosphorus (P) contained in the phospholipids in the form of P=O. These bands were also correlated with the silicon (Si) that was bonded in silicate frustules of cell wall polysaccharide in the form of Si–OH, and to the C−O and C−O−C bonds in carbohydrates. The spectral changes with temperature in this region correlated with the decomposition of silanol silicate frustules. This was also associated with the decomposition of carbon and oxygen bonds in carbohydrates. Subsequently, silicon, carbon, oxygen and hydrogen reacted with alkali metals, such as Ca, Mg and Na, to form new compounds, such as silicon dioxide (SiO_2), hillebrandite ($Ca_2(SiO_3)(OH)_2$), Na_2 (Mg Si)Si_4O_{12}, melilite ($Ca_6Na_2O_{15}Si_4$) and magnesite (Mg CO_3). This will be further discussed in the mineralogical changes section.

Based on the TG, DTG and FTIR spectra (shown in Figures 1 and 2), it can be concluded that *N. oculata* biomass was effectively decomposed by combustion below 800 ˚C. Above 800 ˚C, the ash decomposed, especially at approximately 850 ˚C, as shown in Figure 1.

3.2 Mineralogical changes

The mineralogical change of the sample at each stage of biomass decomposition was observed using X-ray diffracttion (XRD) to study the crystalline species present in the solid residue. The solid sample residual was obtained in the same manner as for the FTIR samples, i.e., biomass was heated from ambient temperature to the end of each stage in accordance with Figure 1. Figure 3 shows the X-ray diffraction patterns of *N. oculata* biomass and the residue, where every sample was acquired from the decomposition of 20 mg of biomass at a 10 °C/min heating rate under a 100 ml/min air flow rate.

Figure 3 shows that the diffraction patterns of biomass and residue at 190 ˚C were nearly identical. The minerals present in the biomass were primarily *aragonite* ($CaCO_3$), *silanetetrayl* (C_8Si), *doyleite* ($Al(OH)_3$), *natrolite* ($Na_2Al_2Si_3O_{10}\cdot 2H_2O$), *magnesium perchlorate dihydrate* ($Cl_2H_8MgO_{12}$) and *silicon dioxide* (SiO_2). The only peak with a change, found at $2\Theta = 31.6^o$, was associated with *antigorite –T* ($Mg_{48}O_{147}Si_{34}$).

The residue at 461 ˚C presented a new diffraction peak at $2\Theta = 23.15^o$ related to $Al_6Ca_9NaO_{18}$. The intensity loss

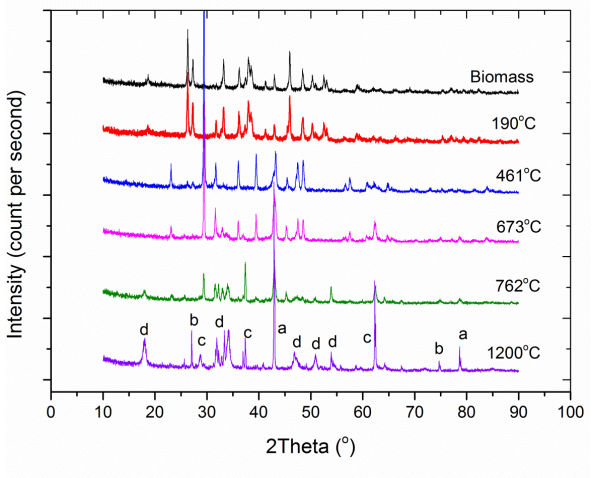

Figure 3. XRD patterns of *N.oculata* biomass and residue after heating to various temperatures a:SiO_2; b:$Ca_2(SiO_3)(OH)_2$; c:$Na_2(MgSi)Si_4O_{12}$; d:$Ca_6Na_2O_{15}Si_4$.

of the two adjacent peaks at 2Θ = 26.34 and 27.32° correlated with the decomposition of *tricalcium silicate* (Ca_3SiO_5). A stronger peak at 2Θ = 29.48° was associated with *dicalcium silicate* (Ca_2SiO_4) or *calcite* ($CaCO_3$). The disappearance of the peak at 2Θ = 33.25° was due to *tricalcium silicate* (Ca_3SiO_5) decomposition. Likewise, *anorthite* ($Al_2CaO_8Si_2$) decomposition results in the loss of peaks at 2Θ = 50.32 and 50.96°.

The diffraction pattern of the residue at 673 ˚C was almost identical with that at 461 ˚C. However, the stronger intensities at 2Θ = 29.41, 42.91, and 62.50˚ were associated with $CaCO_3$, SiO_2 and $Na_2(MgSi)Si_4O_{12}$, respectively. An increase in intensity with combustion temperature was due to increased inorganic content of the residue at higher temperatures (Dodson, Hunt, Budarin, Matharu, & Clark, 2011). The two adjacent peaks at 2Θ = 26.34 and 27.32˚ associated with *tricalcium silicate* were no longer detected.

Figure 3 also shows that the spectrum of the residue at 762 ˚C exhibited decreased intensity at 2Θ = 29.41˚. This was correlated to the decomposition of $CaCO_3$. Additionally, the new compound *melilite* ($Ca_6Na_2O_{15}Si_4$) was formed, which was characterized by the appearance of new peaks at 2Θ = 17.8 and 37.3˚. Moreover, the new and prominent peak at 2Θ = 53.80˚ was also associated with a new compound, i.e., *calcium oxide* (CaO). An extensive discussion regarding *melilite* formation is presented in section 3.3 (morphology and composition of biomass and residue at 1200 ˚C).

The diffraction pattern of the residue at 1200 ˚C showed increased intensities at 2Θ = 17.94, 33.34, 46.78, 50.88 and 53.90˚ (d), caused by the concentration of *melilite* ($Ca_6Na_2O_{15}Si_4$) increasing with temperature. Likewise, an increase in intensity at 2Θ = 42.91 and 78.63° (a) resulted from increased concentration of SiO_2. An intensity increase at 2Θ = 62.30˚ (c) and at 27.04˚ (b) was associated with $Na_2(MgSi)Si_4O_{12}$ and *dicalcium silicate* (Ca_2SiO_5) (in the form of *hillebrandite* ($Ca_2(SiO_3)(OH)_2$)), respectively. The weak intensities at 2Θ = 32.53, 38.81, 46.78, 53.61 and 62.30˚ were associated with $MgCO_3$.

3.3 Morphology and composition of biomass and residue at 1200 ˚C

The material characteristics of biomass and residue at 1200 ˚C were analyzed in terms of their morphology and their composition using SEM and EDX, respectively. Figure 4 shows the morphology of biomass and residue at 1200 ˚C generated by combustion at 10 °C/min heating rate.

Figure 4A-B shows the biomass after drying and pulverization with mortar. The particles were oval-shaped with a fibrous structure (marked with an oval dotted line), with relatively round-shaped fractions of biomass particles having rough and overhanging surface contours (marked with a square dotted line) and particle-like beams with rough and overhanging surface contours (marked with a rectangular dotted line). The remaining particles were small with similar shapes as the larger ones, i.e., oval, relatively round and beam like.

In contrast to the biomass material, the particles of the residue at 1200 ˚C (Figure 4C-D) were more uniform, with a dominantly rhombohedral form. Surface residues also appeared shinier and resembled a star (calcite like).

Changes in the shape and surface of the residue par-ticles were due to the heat treatment. As indicated in Figure 1, most *N. oculata* mass was decomposed by combustion. The onset of biomass decomposition began with the release of moisture and light volatile compounds (Sukarni *et al*., 2015). Subsequent heating caused the matrix structure of the solid particles to soften. The trapped volatiles could cause swollen surfaces, thus changing the shape of the particles (Biagini, Narducci, & Tognotti, 2008). Further heating to higher temperatures degraded chemical bonds and melted some compounds. This destroyed structures of the fibrillar components (cellulose, a polymer of 1,4 linked β-D-glucose) and amorphous materials that composed the cell wall matrix. Furthermore, the cell components evaporated due to heating, and then the volatiles were emitted. Most volatiles were released in the devolatilization stage, leading to rearrangement of chemical bonds, which caused particle shrinkage or even fragmentation or splitting. This formed smaller and more uniform residual fractions.

Figure 4 also indicates that the residue particles had shinier surfaces than the biomass. This was because volatile combustion increased the temperature of solid particles, causing coalescence of graphite nuclei within the solid structures. Furthermore, the internal reactions that occurred in the ash at high temperatures formed colored compounds.

At approximately 850 ˚C, the DTG curve (see Figure 2) showed the last basin during the entire combustion. This was attributable to the decomposition of ash (Sukarni *et al*., 2015). The decomposition that occurred between 850-1200 ˚C was related to the dissociation of alkali carbonate (Arvelakis, Frandsen, Pomeroy, & Dam-Johansen, 2005). The EDX analyses of *N. oculata* biomass (Sukarni *et al*., 2014) indicated that its alkali content was sodium based, whereas potassium was not detected. Hence, the dissociated alkali was predominantly due to Na_2CO_3 degradation. In the range 600-800 ˚C, there was mainly gradual decomposition of $CaCO_3$ (Ali & Strand, 2013) to CaO and CO_2(g). In complex reactions within the ash, the decomposed Na_2CO_3 subsequently reacted with CaO and SiO_2, forming a new compound,

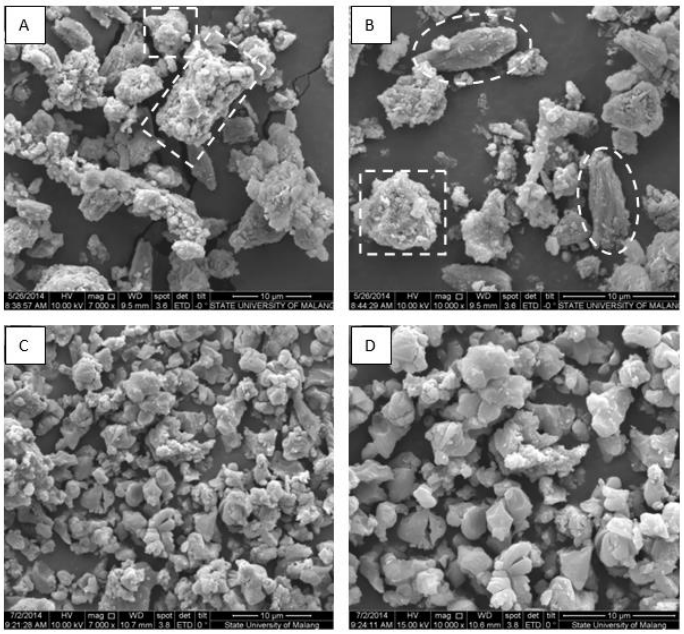

Figure 4. SEM of A: biomass (7000x), B: biomass (10.000x), C: residue at 1200 ºC (7000x), D: residue at 1200 ºC (10.000x). The combustion was performed at the heating rate of 10 ºC/min under 100 ml/min constant air flow rate. Oval dotted line: oval-shaped particles, square dotted line: relatively round shaped particles, rectangular dotted line: beam-like particle.

$Ca_6Na_2O_{15}Si_4$ (*melilite*). The reaction mechanism is shown in Eq. 1.

$$4SiO_2 + 6CaO + Na_2CO_3 \rightarrow Ca_6Na_2O_{15}Si_4 + CO_2(g) \quad (1)$$

Internal reactions occurred in the ash at high temperature via Eq. 1, forming colored compounds. The *melilite* compounds are corroborated by the XRD analysis presented in the previous section.

As specified in Figure 5, a portion of the residue at 1200 ˚C formed agglomerates (indicated by an arrow). This occurred because ash compounds, containing alkali metals (Na) and alkaline earth metals (Ca and Mg), melted and coalesced with silica (Si) at high temperatures (McKendry, 2002). The molten compounds could adhere to the contact area of particles forming particle clusters that were difficult to separate.

Figure 6 shows the elemental composition of biomass and residue at 1200 ˚C originated from 20 mg samples that were observed using EDX spectroscopy. Significant amounts of C and O, 82.46 and 68.32 wt%, respectively, decomposed during the combustion. In agreement with the results of FTIR (Figure 2) and XRD (Figure 3), the remainders of C and O, together with Mg, were bonded to $MgCO_3$, while H and O together with Ca and Si composed a *hillebrandite* compound. The remaining O, together with Na, Ca, Mg and Si was in the compounds $Na_2(MgSi)Si_4O_{12}$, *melilite* ($Ca_6Na_2O_{15}Si_4$) or formed slags such as SiO_2, MgO, and CaO.

According to the analysis of the residue at 1200 ˚C, the byproducts of *N. oculata* biomass combustion include the following compounds: (1) *melilite* compounds, which can be used for glass materials; (2) *silicon dioxide* compounds, which are extensively used as electronics industry raw materials; (3)

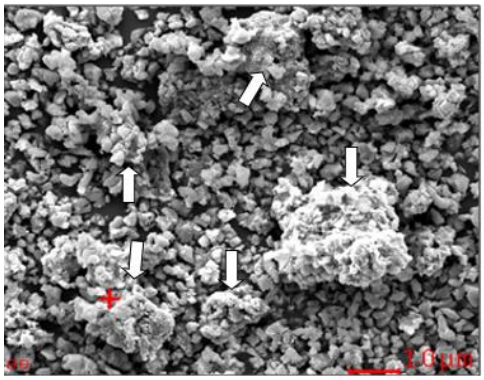

Figure 5. Agglomeration due to melting of alkali and alkaline earth metals is indicated by white arrow.

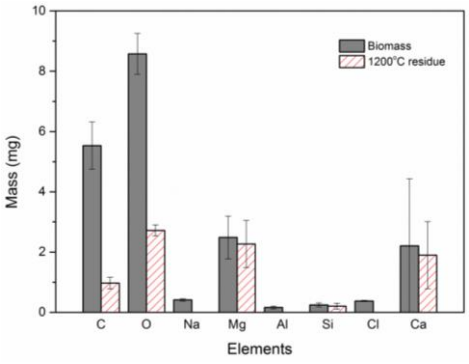

Figure 6. The elemental composition of biomass and 1200 ºC residue as it was observed by using EDX spectroscopy. Error bars indicate standard deviation from three replicates

dicalcium silicate (Ca_2SiO_5), which is one of the essential elements of Portland cement; and (4) *magnesium carbonate*, which was once widely utilized to produce magnesium oxide by calcination. *Magnesite* is also the principal component in refractory bricks and fireproofing. Moreover, the byproducts of *N. oculata* combustion provided a large amount of Mg and Ca (Figure 6), which allows the *N. oculata* residue to serve as an alternative fertilizer.

4. Conclusions

Cellular macromolecular and mineralogical content changes during thermal decomposition of *N. oculata* biomass were examined using FTIR and XRD, respectively. The FTIR and TG results indicated that the decomposition of *N. oculata* biomass effectively occurred below 800 ˚C. Furthermore, the mineral compounds remaining in ash were further degraded at over 800 ˚C. The mineralogical analyses reveal that the mineral compounds in the biomass decomposed and formed new compounds during combustion. Morphological analysis using SEM indicated fragmentation during heating, which created more uniform residue particles at 1200 ˚C. The shinier residue surfaces after heating to 1200 ˚C also indicate the formation of new mineral compounds, mainly *melilite*. This study shows that the use of *N. oculata* as a fuel is feasible and the residual materials obtained from its combustion have potential as feedstocks for various purposes, such as for glass, electronics, Portland cement, refractory bricks, and even fertilizers. Therefore, *N. oculata* is not only a potential energy resource but its combustion could also generate value-added by-products.

Acknowledgements

This research was supported by the Fundamental Research Grant 023.04.1.673,453/2012 from the Directorate General of Higher Education, Republic of Indonesia.

References

Ali, S., & Strand, M. (2013). Melting Characteristics and Morphology of Bottom Ash and Filter Ash of the Circulating Fluidized Bed Boiler. *21st European Biomass Conference and Exhibition*, 1189–1191. 10.5071/21stEUBCE2013-2DV.3.55

Arvelakis, S., Frandsen, F. J., Pomeroy, M., & Dam-Johansen, K. (2005). A Study on the Chemistry of Ash Fractions From MSW Incineration. *13th North American Waste-to-Energy Conference*, 29–42. doi:10.1115/NAWTEC13-3150

Barsanti, L., & Gualtieri, P. (2006). *Algae: anatomy, biochemistry, and biotechnology*. Boca Raton, FL: CRC Press.

Bellamy, L. J. (1975). *The Infra-red Spectra of Complex Molecules*. Dordrecht, Netherlands: Springer Netherlands.

Biagini, E., Narducci, P., & Tognotti, L. (2008). Size and structural characterization of lignin-cellulosic fuels after the rapid devolatilization. *Fuel*, *87*(2), 177–186. doi:10.1016/j.fuel.2007.04.010

Chen, B., Han, X., & Jiang, X. (2016). In-situ FTIR analysis of the evolution of functional groups of oil shale during the pyrolysis. *Energy Fuels*, *30*(7), 5611–5616. doi:10.1021/acs.energyfuels.6b00885

Chen, C., Ma, X., & Liu, K. (2011). Thermogravimetric analysis of microalgae combustion under different oxygen supply concentrations. *Applied Energy*, *88*(9), 3189–3196. doi:10.1016/j.apenergy.2011.03.003

Converti, A., Casazza, A. a., Ortiz, E. Y., Perego, P., & Del Borghi, M. (2009). Effect of temperature and nitrogen concentration on the growth and lipid content of Nannochloropsis oculata and Chlorella vulgaris for biodiesel production. *Chemical Engineering and Processing: Process Intensification*, *48*(6), 1146–1151.

de Morais, M. G., & Costa, J. A. V. (2007). Biofixation of carbon dioxide by Spirulina sp. and Scenedesmus obliquus cultivated in a three-stage serial tubular photobioreactor. *Journal of Biotechnology*, *129*(3), 439–445. doi:10.1016/j.jbiotec.2007.01.009

Demirbas, A. (2010). Use of algae as biofuel sources. *Energy Conversion and Management*, *51*(12), 2738–2749. doi:10.1016/j.enconman.2010.06.010

Dodson, J. R., Hunt, A. J., Budarin, V. L., Matharu, A. S., & Clark, J. H. (2011). The chemical value of wheat straw combustion residues. *RSC Advances*, *1*(3), 523. doi:10.1039/c1ra00271f

Duygu, D. Y., Udoh, A. U., Ozer, T. B., Akbulut, A., Acikgoz, I., Yildiz, K., & Guler, D. (2012). Fourier transform infrared (FTIR) spectroscopy for identification of Chlorella vulgaris Beijerinck 1890 and Scenedesmus obliquus (Turpin) Kützing 1833. *African Journal of Biotechnology*, *11*(16), 3817–3824.

García-González, M., Moreno, J., Manzano, J. C., Florencio, F. J., & Guerrero, M. G. (2005). Production of Dunaliella salina biomass rich in 9-cis-beta-carotene and lutein in a closed tubular photobioreactor. *Journal of Biotechnology*, *115*(1), 81–90. doi:10.1016/j.jbiotec.2004.07.010

Griffiths, M. J., & Harrison, S. T. L. (2009). Lipid productivity as a key characteristic for choosing algal species for biodiesel production. *Journal of Applied Phycology*, *21*(5), 493–507. doi:10.1007/s10811-008-9392-7

Hibberd, D. J. (1981). Notes on the taxonomy and nomenclature of the algal classes Eustigmatophyceae and Tribophyceae (synonym Xanthophyceae). *Botanical Journal of the Linnean Society*, *82*(2), 93–119. doi:10.1111/j.1095-8339.1981.tb00954.x

Hu, H., & Gao, K. (2003). Optimization of growth and fatty acid composition of a unicellular marine picoplankton, Nannochloropsis sp., with enriched carbon sources. *Biotechnology Letters*, *25*(5), 421–425.

López-González, D., Fernandez-Lopez, M., Valverde, J. L., & Sanchez-Silva, L. (2014). Kinetic analysis and thermal characterization of the microalgae combustion process by thermal analysis coupled to mass spectrometry. *Applied Energy*, *114*, 227–237. doi:10.1016/j.apenergy.2013.09.055

McKendry, P. (2002). Energy production from biomass (part 1): Overview of biomass. *Bioresource Technology*, *83*(1), 37–46. doi:10.1016/S0960-8524(01)00118-3

Peng, F. U., Song, H. U., Jun, X., Lushi, S. U. N., Tao, Y., Anchao, Z., & Junying, Z. (2009). Mechanism Study of Rice Straw Pyrolysis by Fourier Transform. *Chinese Journal of Chemical Engineering*, *17*(3), 522–529.

Sukarni, Sudjito, Hamidi, N., Yanuhar, U., & Wardana, I. N. G. (2014). Potential and properties of marine microalgae Nannochloropsis oculata as biomass fuel feedstock. *International Journal of Energy and Environmental Engineering*, *5*(4), 279–290. doi:10.1007/s40095-014-0138-9

Sukarni, Sudjito, Hamidi, N., Yanuhar, U., & Wardana, I. N. G. (2015). Thermogravimetric kinetic analysis of Nannochloropsis oculata combustion in air atmosphere. *Frontiers in Energy*, *9*(2), 125–133. doi:10.1007/s11708-015-0346-x

Tahmasebi, A., Kassim, M. A., Yu, J., & Bhattacharya, S. (2013). Thermogravimetric study of the combustion of Tetraselmis suecica microalgae and its blend with a Victorian brown coal in O2/N2 and O2/CO2 atmospheres. *Bioresource Technology*, *150*, 15–27. doi:10.1016/j.biortech.2013.09.113

Yusuf, C. (2007). Biodiesel from microalgae. *Biotechnology Advances*, *25*(3), 294–306. doi:10.1016/j.biotechadv.2007.02.001